

Tuning NMC Structure via Calcination: Insights from Powder X-Ray Diffraction

Natalia Firlej, Dominika A. Buchberger,* Magdalena Winkowska-Struzik, Krzysztof Gadomski, Alicja Głaszczka, Michał Grygiel, Tomasz K. Pietrzak, and Andrzej Czerwiński

The electrochemical performance of $\text{LiNi}_x\text{Mn}_y\text{Co}_z\text{O}_2$ (NMC) materials depends strongly on their composition and structure. This study investigates the influence of calcination temperature on the structural, morphological, and electrochemical properties of various NMC materials. For the first time, a conventional powder X-ray diffractometer is used for *in situ* analysis of NMC calcination, revealing a four-stage transition from precursor to hexagonal structure and composition-dependent transition temperatures. This accessible method offers advantages over synchrotron-based techniques. *In situ* X-ray diffraction (XRD) enables

selection of annealing temperatures for *ex situ* studies, which are correlated with electrochemical behavior using scanning electron microscopy, XRD, and chronopotentiometry. Raman mapping, which has not previously been applied in this manner, provides novel insight into the local structure and stability of the material. Additionally, the role of calcination atmosphere in Ni-rich NMCs is examined. The results guide further development of advanced NMCs, including core-shell materials, and demonstrate the practicality of laboratory-based structural methods for broader materials research.

1. Introduction

Lithium-ion batteries are the leading choice for portable electronics, electric vehicles, and energy storage due to their high energy density and power output.^[1] Since Sony's commercial launch in 1991, battery energy density has nearly quadrupled thanks to improvements in cell chemistry and manufacturing.^[2] Among cathode materials, lithium nickel manganese cobalt oxides ($\text{Li}(\text{Ni}_x\text{Mn}_y\text{Co}_z)\text{O}_2$, where $x + y + z = 1$), are widely used for their high energy density and relatively low cost. NMCs are solid solutions of LiCoO_2 (LCO), LiNiO_2 (LNO), and LiMnO_2 (LMO),^[3,4] with each component offering unique benefits: nickel and manganese lower the active material cost, cobalt provides structural stability and reduces lithium-nickel cation mixing,^[5] while manganese improves thermal and cycling stability.^[6] Among many options available, no middle ground was observed for NMC compound,^[3] since batteries' electrochemical and safety properties depend much upon cathode materials. The research continues into more advanced structures, such as gradient cathodes with nickel-rich cores and manganese/cobalt-rich shells.^[7,8] Although, optimizing these materials requires precise calcination studies.

Variable-temperature X-ray diffraction (VT-XRD) is one of the key techniques for analyzing structural changes during synthesis.^[9,10] It enables *in situ* monitoring of phase transitions, intermediate phases, and thermal stability—critical for optimizing cathode materials for electrochemical performance.^[11] There are few thermal XRD studies on the calcination of various NMC and analogous materials. One of the first investigations focused on the synthesis and decomposition of LiNiO_2 (LNO) using *in situ* synchrotron XRD at $3\text{ }^\circ\text{C min}^{-1}$ heating rate and pure oxygen gas.^[12] Bianchini et al. studied the calcination and decomposition mechanism and distinguished the preannealing step with the formation of the NiO cubic rock-salt (RS) structure and four calcination regions: 1) rock-salt phase (up to $436\text{ }^\circ\text{C}$), 2) defective LNO: preferential Li layer and Ni vacancies formations (up to $517\text{ }^\circ\text{C}$), 3) layered phase: cation migration and layering (up to $604\text{ }^\circ\text{C}$), and 4) regular LNO: LiOH fully consumed (up to $700\text{ }^\circ\text{C}$). The LNO decomposition at prolonged $700\text{ }^\circ\text{C}$ and higher temperatures in air and pure O_2 was also studied. Further studies on pure and doped LNO materials focused on Li source choice (LiOH vs Li_2CO_3).^[13] Measurements were performed using the hard X-ray synchrotron beamline on samples preheated under oxygen to $480\text{ }^\circ\text{C}$ ($10\text{ }^\circ\text{C min}^{-1}$ ramp, 3 hr dwell), and then *in situ* heated at $10\text{ }^\circ\text{C min}^{-1}$ ramp rate in a pure oxygen environment. Diffraction peaks from crucible material overlapped with few important LNO peaks thus only two 2θ regions were analyzed. It was shown, that LNO layered structure is formed at a much higher temperature for Li_2CO_3 reaction with Ni(OH)_2 ($775\text{ }^\circ\text{C}$) than the similar reaction with LiOH ($575\text{ }^\circ\text{C}$). The most recent study using combined (XAS) X-ray absorption spectroscopy and XRD performed at synchrotron beamline at ultra-pure air with $10\text{ }^\circ\text{C min}^{-1}$ heating rate claims that there is an early nucleation of the layered LNO alongside lithiated RS directly from the decomposed Ni(OH)_2 .^[14] This phase coexistence is suggested

N. Firlej, D. A. Buchberger, M. Winkowska-Struzik, K. Gadomski, A. Głaszczka, M. Grygiel, A. Czerwiński

Faculty of Chemistry
University of Warsaw

Pasteura 1, 02-093 Warsaw, Poland
E-mail: d.buchberger@uw.edu.pl

K. Gadomski, T. K. Pietrzak
Faculty of Physics
Warsaw University of Technology
Koszykowa 75, 00-662 Warsaw, Poland

 Supporting information for this article is available on the WWW under <https://doi.org/10.1002/batt.202500380>

to occur between 210 and 760 °C. Above 760 °C, it is claimed that LNO starts to degrade, which is contrary to Bianchini et al. (700 °C).^[12] These differences in decomposition temperature might be connected to calibration and/or heating rate chosen for each experiment or differences in the reaction atmosphere. The decomposition was observed at a higher temperature, which might suggest the non-equilibrium state during the measurement with a faster heating rate.

Similarly to LNO, LiCoO₂ (LCO) was also investigated using in situ synchrotron XRD.^[15] Data sets for Co(OH)₂/LiOH and Co₃O₄/LiOH mixtures were recorded at a heating rate of 3 °C min⁻¹ with the airflow. When using cobalt hydroxide as a Co precursor there are several transitions observed: from (I) Co(OH)₂ to CoOOH then (II) through spinel up to (III) layered structure. In the case of the Co₃O₄ precursor, the transition starts from the initial spinel through lithiated spinel to finally overlap with the layered structure. Since both experiments were carried out up to 700 °C, the pure LCO phase was not achieved. The authors suggest that lowering the calcination temperature will significantly impact the electrochemical performance of a Co-rich coated cathode.^[15]

In the case of NMC materials, two investigations have been reported. The first one discussed the synthesis of LiNi_{0.8}Mn_{0.1}Co_{0.1}O₂ (NMC811) material,^[16] and the second comparison between NMC111 and NMC811 syntheses.^[17] Wolfman et al. studied their sample in two scenarios: 1) using preheated Ni_{0.8}Mn_{0.1}Co_{0.1}(OH)₂ precursor at 350 °C in O₂ to form rock-salt structure and then calcinated it with LiOH, and 2) using the conventional method, where Ni_{0.8}Mn_{0.1}Co_{0.1}(OH)₂ and LiOH were calcinated directly.^[16] Samples were calcinated using in situ synchrotron XRD at 2 °C min⁻¹ to 500 °C and held at 500 °C for 90 min, then heated at 5 °C min⁻¹ to 800 °C. Surprisingly, the conventional heating did not result in well-crystallized NMC811 at the end of the in situ heating (minor (003) and no (101) or (006) reflexes were seen). However, when pre-heated transition metal oxide precursor and LiOH were used a better layering was observed. At 700 °C, the authors claimed the possible Li loss and structure disorder.

In contrast, Ying et al. showed the comparison of NMC111 and NMC811 calcination using in situ synchrotron XRD.^[17] In the case of NCM811, O₂ was flushed through the tube upon calcination, while for NCM111, the tube was left open to the air. In both cases, samples were heated up to 800 °C. The authors suggest three structural transitions during the calcination of NMC811 (P-3m1 → Fm-3 m → disordered R-3 m → R-3m) and two transitions for NMC111 (no cubic phase). A more surprising is that authors observed the existence of Li₂CO₃ crystals much above its melting point (ca. 75 °C higher), which might be caused by the sample underheating in the used set-up (lower temperature at the sample compared to the location of the controller thermocouple). Thus the shown in situ XRD heat maps might be shifted by ca. 75 °C, and this has to be taken into account when comparing future results.

In conclusion, VT-XRD on precursor materials offers valuable insight into thermal behavior, phase transitions, and structural evolution, essential for optimizing synthesis and predicting electrochemical performance. In this study, we synthesized and

analyzed NMC111, NMC622, and NMC811 compositions prepared at different temperatures, linking their structure to electrochemical behavior. This is the first comprehensive use of a conventional powder diffractometer in in situ mode to study phase transitions across different NMCs. Based on the results, we proposed a calcination mechanism and prepared and analyzed ex situ samples. We also compared conventional XRD with synchrotron methods. Complementary characterization included scanning electron microscopy (SEM), electrochemical testing, and, for the first time, Raman mapping to study local structure and thermal degradation. For NMC811, we explored the influence of air versus oxygen atmospheres. The combined approach revealed how crystal structure and morphology impact performance and demonstrated the usefulness of accessible lab-scale structural tools.

2. Results and Discussion

2.1. NMC Formation Mechanism Studied by In Situ XRD Analysis

In situ XRD enabled the observation of structural changes during the crucial thermal treatment stage of NMC synthesis. According to the literature, different calcination temperatures are used depending on the elemental composition of NMC materials.^[4] Those with higher nickel content are calcined at lower temperatures due to the observed structure decomposition during the synthesis process.^[18] This in situ method offered detailed insights into phase evolution and crystalline transformations across temperature ranges.

Figure 1 shows three heating maps from the NMC precursor stage up to the formation of NMC hexagonal structures for NMC111, NMC622, and NMC811 (the stage calibration and the diffractograms of the NMC precursors are presented in Figure S1 and S2 of Supporting Information); we can observe some differences depending on Ni content in the initial precursor since they are mixtures of different TM hydroxides. The pure Ni(OH)₂, Mn(OH)₂, and Co(OH)₂ annealing steps are shown in Figure S3, Supporting Information and discussed in Supporting Information. Based on the VT-XRD results of NMC111, NMC622, and NMC811 precursors, the heating process can be divided into four stages marked in Figure 1 and S4 and schematically shown in Figure 2. The first stage consists of the initial broader reflexes arising from transition metal (TM) hydroxides of trigonal structure (P -3 m 1 space group) of NMC precursors with the narrow reflexes corresponding to larger LiOH crystallites of tetragonal structure (P 4/n m m space group). It is worth noting that TM hydroxides have a layered structure with a ca. 4.6 Å slab where OH⁻ groups alternate up and down. During the heating process, the lattice parameters decrease causing the layers to get closer together and thus initiating OH⁻ groups reaction forming H₂O vapors that escape the hydroxide structure. The phase formation mechanism depends on the nickel content. In the case of NMC111 precursor, the spinel-like structure (space group F d -3 m) is revealed at approximately 275 °C (Figure S5, Supporting Information). This observation is further validated

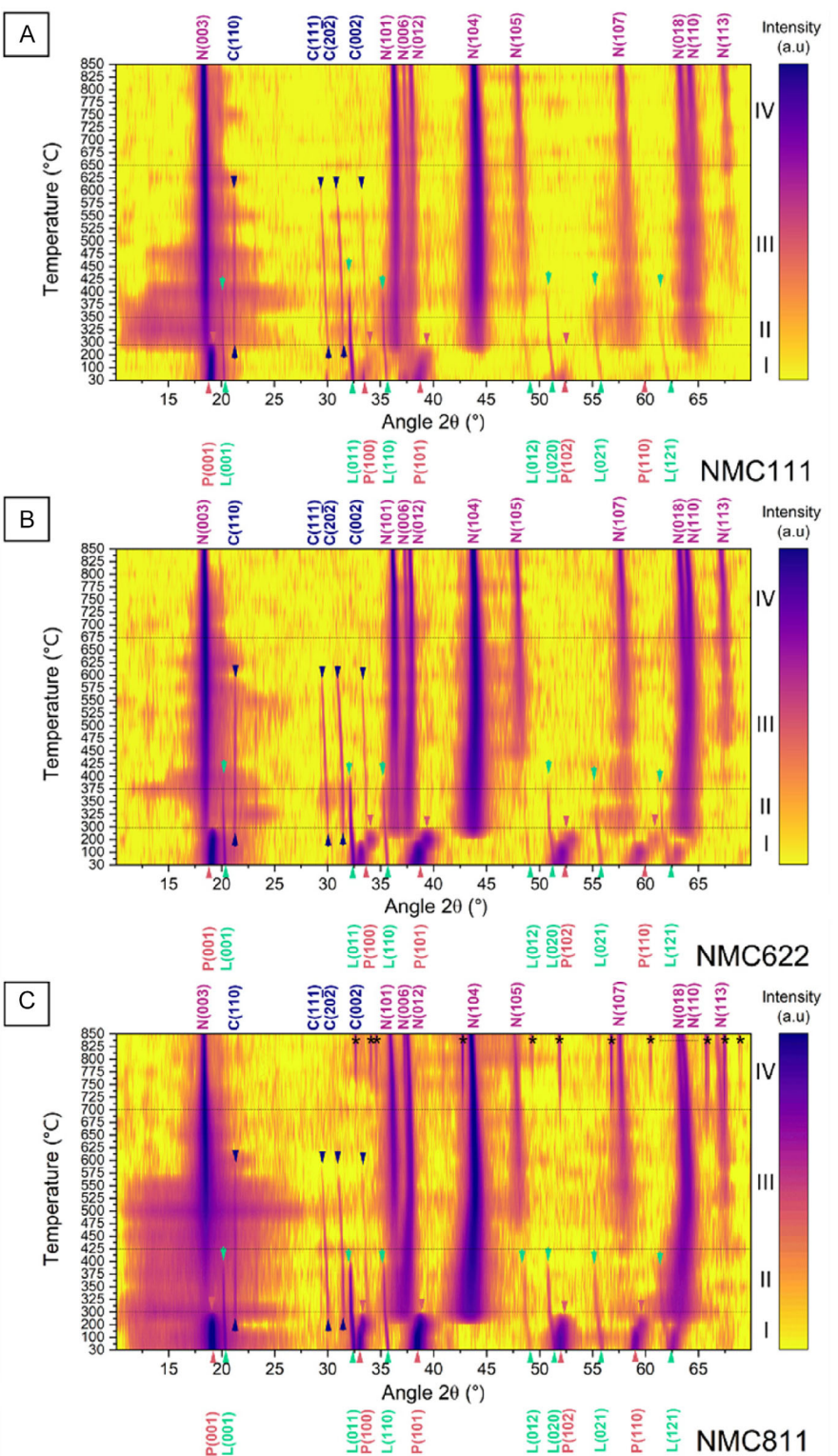


Figure 1. Temperature-dependent XRD of A) NMC111, B) NMC622, and C) NMC811 cathode powder precursors. P—NMC111-OH precursor, L—LiOH, C— Li_2CO_3 , N—NMC final materials. Graphs in log2 scale. Asterisks—planes from oven holder after sample contraction. Horizontal short-dashed lines indicating three transition temperatures (T_1 , T_2 , and T_3).

by Raman spectroscopy (Figure S6, Supporting Information). It has been demonstrated that $\text{Mn}(\text{OH})_2$ and $\text{Co}(\text{OH})_2$ ^[15] precursors exhibit a comparable mechanism. This observation indicates that

for low Ni content NMC materials, the second step of annealing generally requires the formation of spinel-like structure in the presence of oxygen. The presence of numerous vacancies in

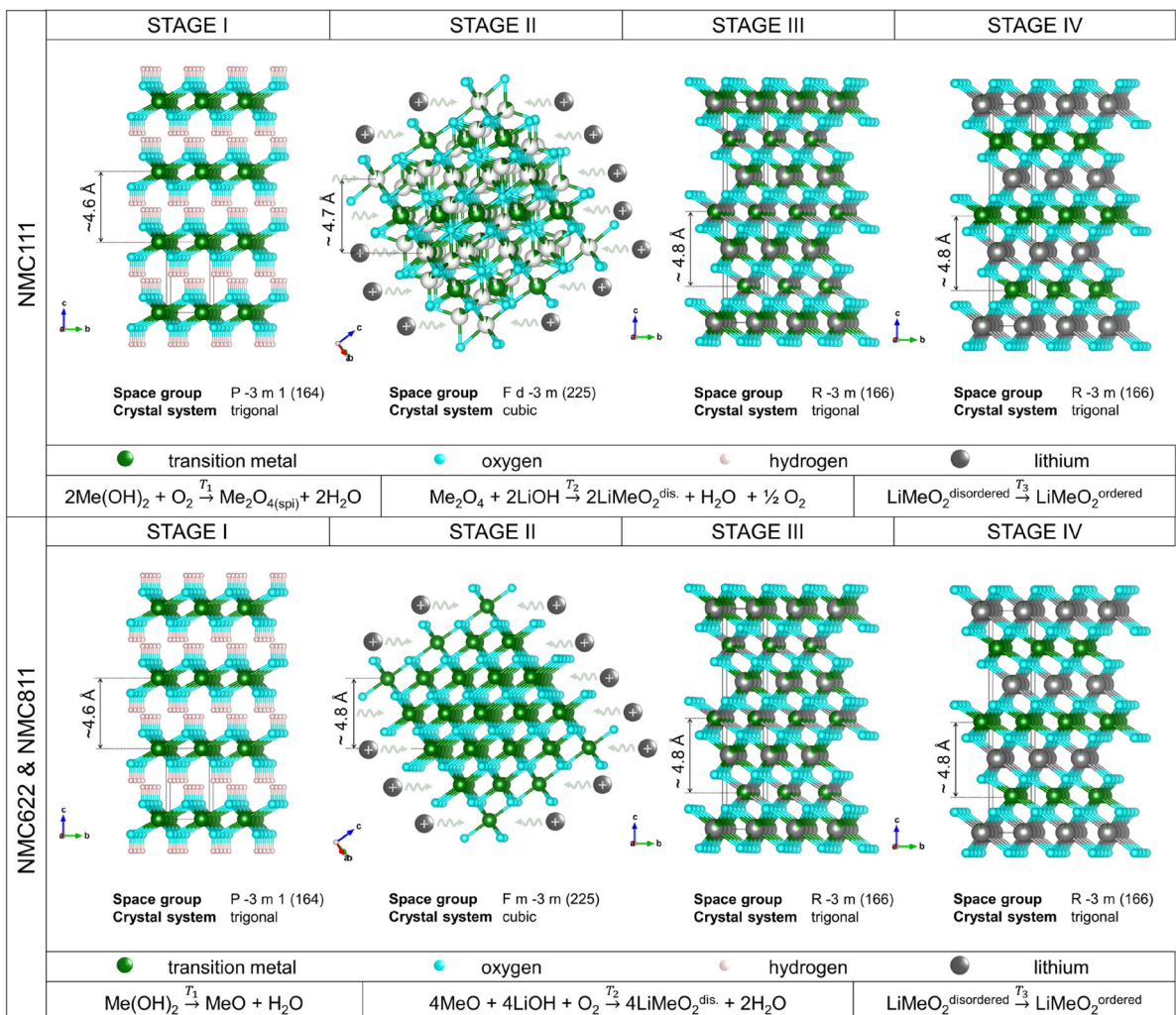


Figure 2. Schematics of thermal transformation of transition metal (Me) hydroxides into lithiated transition metal oxides involving four stages and chemical reactions based on three transition temperatures (T_1 , T_2 , and T_3) for low-Ni and high-Ni content.

the small spinel crystals facilitates the diffusion of lithium ions into the crystal structure, thus enabling early lithiation of the material. It is noteworthy that this particular sample exhibited the least significant macroscopic volume change showing that the reaction mechanism based on spinel framework at stage II differs from Ni-rich materials (Figure 2). NMC622 and, most notably, NMC811 demonstrated substantial volume change and pellet cracking (Figure S7). This phenomenon can be attributed to the unique nature of nickel-rich materials. Similarly to $\text{Ni}(\text{OH})_2$,^[12] the annealing process of Ni-rich precursors gives rise to the formation of a cubic NiO-like structure, commonly known as a rock-salt structure (space group F m -3 m). The existence of the rock-salt phase (possibly lithiated analogously to $\text{Li}_{0.3}\text{Ni}_{0.7}\text{O}$)^[19] was confirmed for NMC622 and NMC811 (Figure 3A). NiO-like structure exists the longest for NMC811 sample (stage II). At ca. 300 °C, we can observe a partial reaction of LiOH with CO_2 from the air and the formation of Li_2CO_3 particles or as suggested by Ying et al. it crystallized from an amorphous Li_2CO_3 layer attached to LiOH crystals.^[17]

The disordered NMC-like structure forms early on as the defective rhombohedral (Ni-rich) or hexagonal (Ni-poor) phase and co-exists with NiO-type structure at different concentrations for higher Ni contents or transforms from spinel structure as seen for low Ni content (Figure 3A). It is clear that the stage II transition from hydroxide to cubic phase is an intermediate reaction step for all types of NMC materials. In the case of NMC111, the cubic spinel structure starts to form around 225 °C (T_1) and quickly disappears (around 350 °C— T_2) leaving only a disordered hexagonal structure which becomes more ordered with a higher lithiation level (stage III). Stage III is a very important step where the lithiation and oxidation of TM oxides progress. Only the NMC111 precursor seems to quickly advance into the disordered hexagonal phase. The full transformation into the disordered hexagonal structure appears at ca. 375 °C for NMC622, and it develops across stage III. This process takes the longest in the case of NMC811, where the rhombohedral phase co-exists with the cubic phase until 425 °C. The disordered hexagonal phase can be distinguished above 550 °C. At lower temperatures (003) reflexes of

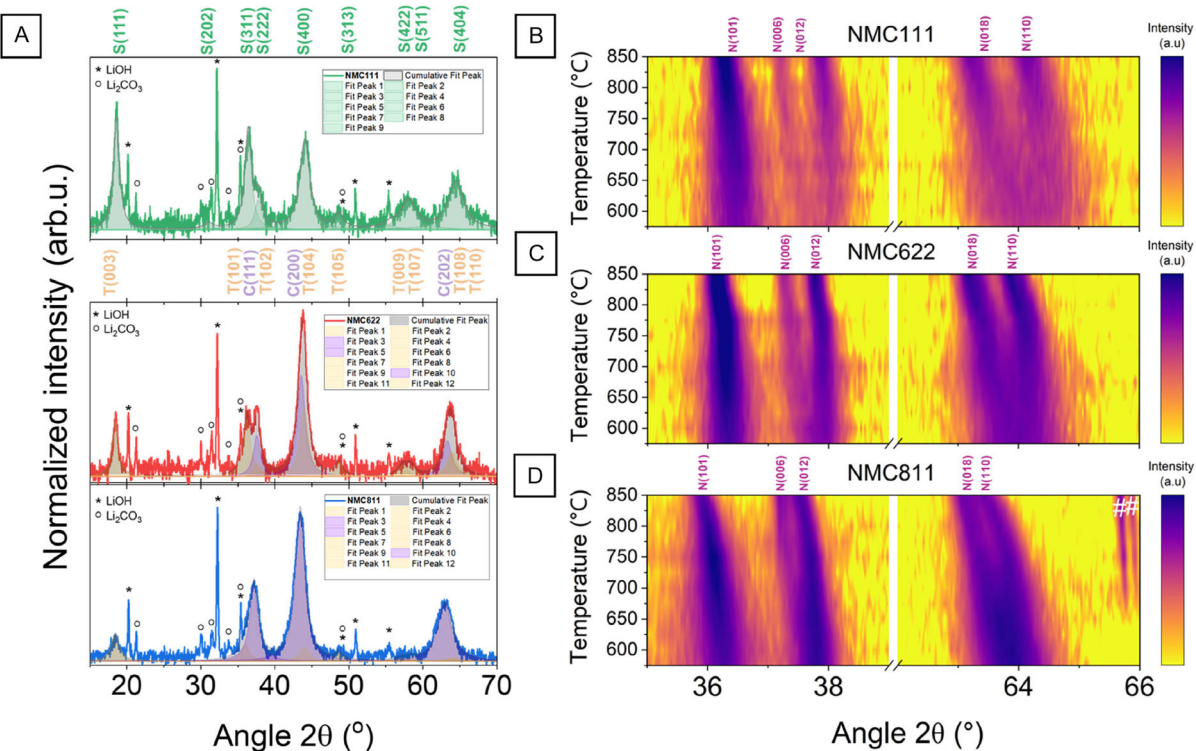


Figure 3. A) XRD diffractogram of NMC111 precursor shows a spinel-like cubic phase at 300 °C, and XRD diffractograms of NMC622, and NMC811 precursors show a coexistence of the cubic NiO-type phase at 300 °C C) and disordered trigonal NMC-like phase (T). Temperature-dependent XRD of B) NMC111, (C) NMC622, and D) NMC811 cathode powder precursors. T—disordered Li_xMeO_2 phase, C—NiO-like cubic phase, S—spinel-like cubic phase. Graphs (B–D) in log2 scale. Number sign (#)—planes from oven holder after sample contraction.

disordered layered structures are much smaller than (104) plane showing a defective nature of the structure due to its low Li content at those temperatures. With further annealing the (003) reflex gains intensity, whereas (101) and (012) reflexes well separate. This correlates with the disappearance of Li compounds. LiOH intensity fades just before its melting point for NMC111 (at ca. 450 °C) and a bit earlier for NMC622 and NMC811 (at ca. 400 °C) indicating a slow but progressing solid-state reaction between TM hydroxide and LiOH mixture. In contrast, the Li_2CO_3 disappears at 625 °C and 600 °C for NMC111 and Ni-rich NMCs, respectively, suggesting that at that temperature and in an O₂-rich atmosphere, all Li⁺ ions diffuse into disordered NMC structures. In this temperature range, very broad peaks of NMC tend to narrow as temperature increases.

A few tens of degrees higher the mixed Li and TM ions in 3a and 3b positions start to reorganize within the hexagonal structure and take their favorable positions: 3a—Li and 3b—TM. This is evident in the heatmaps where two doublets: (006)/(012) and (018)/(110) visibly separate confirming the creation of the Li—O—TM sequence of layers (stage IV). Figure 3B–3D shows that the beginning temperature of the doublets' separation (T_3) is characteristic for different Ni contents, lower for Ni-poor (625–650 °C) and higher for Ni-rich samples (650–675 for NMC622 and 700–725 °C for NMC811). What is interesting, we observe that excessive temperatures might cause deterioration of the NMC811 hexagonal structure, which manifests in slight doublets peak

merging just above 800 °C, but also the growth of the peak originating from (104) plane with the simultaneous fading of the peak originating from (003) plane. These XRD features suggest the formation of another disorder, probably towards the cubic phase, which is similar to LiNiO_2 behavior.^[12] Additionally, we observed the shrinkage of that sample and thus the diffraction peaks coming from the holder can be visible in Figure 1 and 3D. The full sample holder diffractogram is shown in Figure S8, Supporting Information.

2.2. Calcination Temperature Dependence on NMC Structures

Consequently, three calcination temperatures within the range of stage IV from the previous experiment (750, 800, and 850 °C) were chosen for further in-depth investigation. This research aimed to achieve a well-defined and high-quality hexagonal structure in various NMC cathode materials and to correlate their structural parameters with electrochemical performance. The crystal structure of the obtained materials was identified using recorded X-ray diffractograms. All of the synthesized materials demonstrated an $\alpha\text{-NaFeO}_2$ -type layered structure, which belongs to the R-3 m space group in the hexagonal system (stage IV), as shown in Figure 4. Crystallite sizes were determined based on the analysis of the resulting diffraction patterns and further discussed and compared with SEM images. It is worth noting that there is a

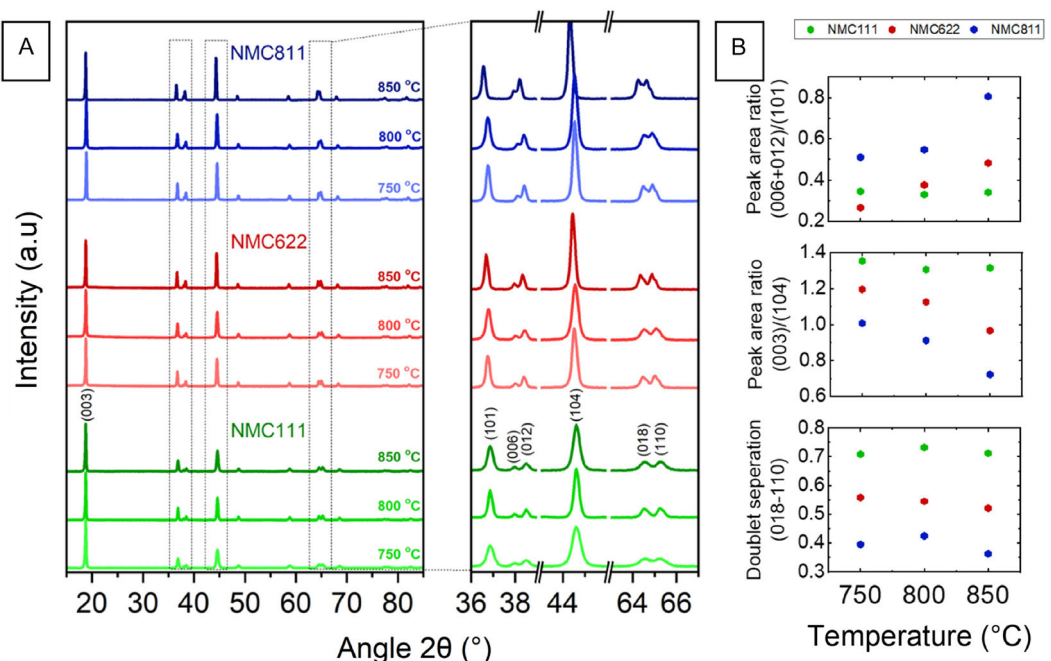


Figure 4. A) XRD patterns of NMC111, NMC622, and NMC811 materials annealed at 750, 800, and 850 °C; B) calculated values of the ratio of integral intensities (003)/(104), the ratio of integral intensities (006 + 102)/(101), and doublet separation (018–110) for NMC111, NMC622, and NMC811 cathode powders.

difference between the reflex positions observed in in situ patterns and those observed ex situ due to thermal expansion of the crystals at elevated temperatures. Therefore, the patterns that were recorded in situ demonstrate all reflections exhibit a shift towards lower angles. Furthermore, an alteration in the macroscopic sample volume was observed (Figure S7, Supporting Information), resulting in a high background change in low angles at elevated temperatures, particularly in Ni-rich samples. It is clear that these thermal effects are certainly avoided in ex situ samples, which allows for further comprehensive analysis.

A high-quality hexagonal structure in NMC is desirable as it influences the electrochemical properties and contributes to the overall stability and efficiency of the cathode material. A well-defined and ordered hexagonal structure enhances the material's structural integrity during repeated charge–discharge cycles, ensuring prolonged battery life and reliability.^[20] It also facilitates efficient lithium-ion diffusion within the crystal lattice, promoting improved electrochemical performance. Structural imperfections may result in reduced capacity, decreased cycling stability, and hindered lithium-ion mobility. Consequently, the quality of the hexagonal structure in NMC is a critical factor in determining its suitability for high-performance lithium-ion batteries.^[21]

Various parameters may determine the quality of the hexagonal structure, but the literature commonly indicates that the most significant and measurable are the ratio of integral intensities of reflexes coming from planes (003)/(104), ratio of integral intensities (006 + 102)/(101), and the reflex resolution (018–110). All the planes mentioned above are presented in Figure S9, Supporting Information. The desired ratio of the integral intensity of reflections coming from the planes (003) and (104) (I_{003}/I_{104})

should exceed 1.2,^[22] accompanied by as small as possible integrated intensity ratio of (006)+(012)/(101)^[23] corresponds to minimal $\text{Ni}^{2+}/\text{Li}^+$ cation mixing.^[24,25] This structure deterioration is based on a small difference in ionic radii of Ni^{2+} and Li^+ , being 0.69 and 0.76 Å, respectively. The partial residency of lithium ions in Ni^{2+} locations creates cation mixing in the material lattice structure, which causes the disturbance of Li^+ diffusion routes.^[26] Furthermore, (018–110) doublet separation, expressed by the difference of peak position (2θ angle value), is also significant as it refers to a better hexagonal ordering, meaning whether the oxygens are in their proper hexagonal close packing structure.^[23] The values of all these parameters are presented in Figure 4B.

Once the annealing temperature rises, peaks become more distinct and narrower with changes in doublet separations at higher angles, which suggests progressive crystallization of the layered structure and bigger particle size. Based on the parameters calculated, we see that NMC111 tested in all three temperatures resulted in obtaining final powders with similar crystalline properties and fit in the description of the optimal hexagonal ordering. The only significantly different parameter is the crystal size as discussed below. For NMC622, the proper (003)/(104) ratio value was obtained for samples calcined at 750 and 800 °C, while the material synthesized at 750 °C shows a lower ratio of (006) and (012) to (101) and a higher resolution of the (018–110) doublet, which suggests that the lowest temperature gives a more accurate hexagonal structure. The third material, NMC811, showed slightly above the satisfying value of (003)/(104) ratio when calcined at 750 °C, although other calculated parameters showed uncertain values suggesting disturbance of the optimal hexagonal ordering for all measured NMC811 samples. This trend was intensified with increasing temperatures. Overall, there is a

tendency for deterioration with increasing Ni content for all three parameters discussed above.

We also studied the local structure distribution of obtained materials using Raman microspectroscopy. For this, we performed Raman mapping and analyzed the spectral changes within the full data set (**Figure 5**). The biggest differences are recorded for NMC811, where the spectra intensively change across increasing temperatures. At 850 °C, the map is nonuniform with big differences between map points. Corresponding spectra show a clear phase change from hexagonal (light blue) to another phase (possibly spinel—a black spectrum). A similar trend is visible in NMC622 where the black spectrum is almost like that of NMC811 (different TM concentrations influence the position and intensity of Raman lines in both structures), although the degree of this effect at 850 °C is much smaller. The new Raman features appear at 581 and 520 cm⁻¹ and progress into 587 (strong) and 527 cm⁻¹ (weak) for NMC811. In the case of NMC622, similar features develop at 513 and 589 cm⁻¹. Even though NMC111 samples seem the most structurally stable in all three temperatures, we can see that the spectra slightly change. When normalizing the spectra to A_{1g} mode (597 cm⁻¹), it is obvious that E_g mode (480 cm⁻¹) gets a bit smaller for a higher temperature which suggests the small atom rearrangement.

Based on the results obtained, we can conclude that for each of the materials, calcination conditions should be individually tailored. Outside the optimal temperature range, the crystallographic structure is not yet properly formed for too low temperatures and undergoes deterioration and progressive phase transition for excessively high temperatures.

2.3. Morphological Studies of NMC Precursors and Final Materials

SEM was used to explore the morphologies of the prepared powders, both before and after calcination at different temperatures. Features such as grain size and surface characteristics, including mechanical failure, have a strong influence on overall material properties^[27] Dimensions of primary particles influence the surface area, which further contributes to discharge capacities because the increase in grain size might limit Li⁺ diffusion in NMC material.^[28]

The TM hydroxides' particles presented in **Figure 6** are characterized by a flaky morphology. Once those materials are calcinated the particles become thicker and rounded and closely agglomerated. In general, NMC particles have irregular shapes and changes in width correlated to differences in calcination temperature adopted. For NMC111, the smallest particles are observed for 750 °C (40–300 nm), whereas for 850 °C they reach ca. 100–600 nm revealing a continuous growth in this temperature range (**Figure 7A**). For higher Ni content, the particles' growth is faster showing bigger particles at the same calcination temperatures (stage IV is where the calcination becomes a sintering process). For instance, NMC811 showed the biggest particles of over 1-micron size with well-formed facets at 850 °C. Moreover, in all of the materials partial agglomeration becomes evident, introducing a complexity to the microstructure. Additionally, the SEM images of Ni-rich NMCs calcinated at higher temperatures have shown the formation of bipyramid-shaped crystallites, which are associated with preferable particle growth.^[29,30]

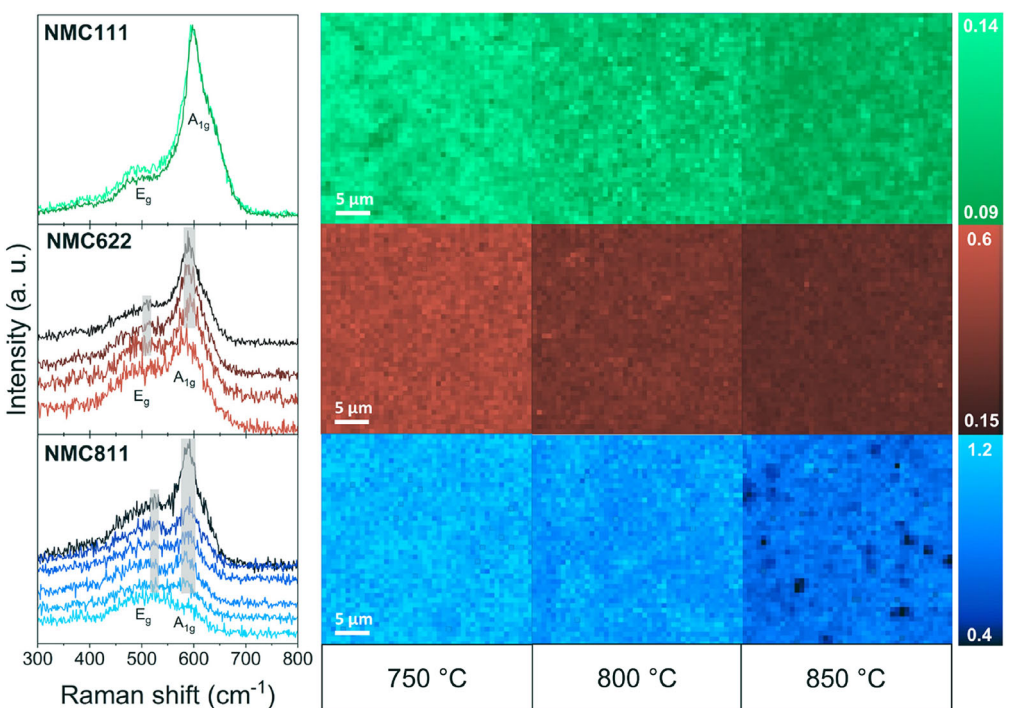


Figure 5. Raman maps and corresponding-colored spectra of NMC111, NMC622, and NMC811 materials annealed at 750, 800, and 850 °C. The spectral changes are represented by the ratio between two selected peaks.

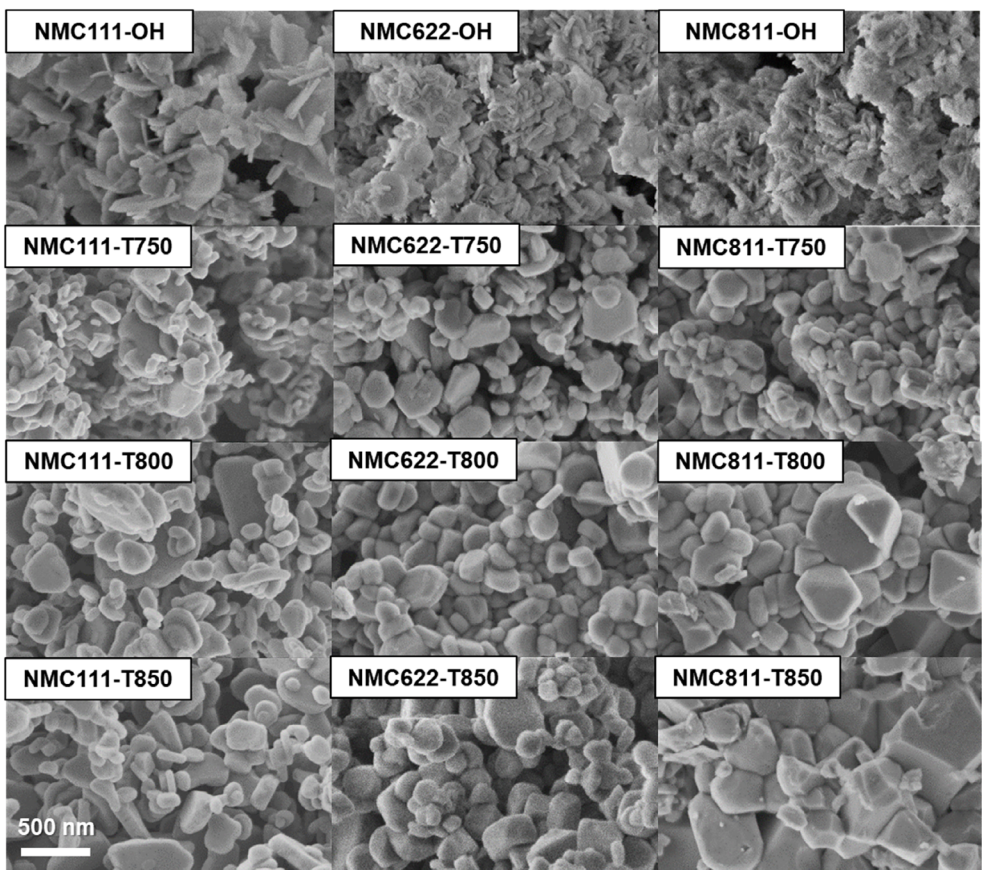


Figure 6. SEM images of NMC111, NMC622, and NMC811 precursors and cathode materials synthesized at different temperatures.

The particle sizes observed on the SEM images are correlated with the average size of the crystallites obtained from X-ray diffractograms. The average crystallite sizes were calculated using the Scherer equation based on the diffraction peaks originating from plates (101), (006), (012), (104), and (015). For each sample, the relationship was plotted as a function of annealing temperature in Figure 7B. For all three materials, we observed an increase in crystallite size when a higher calcination temperature was applied, ranging from 31 nm to 64 nm for NMC111, 51 to 94 nm for NMC622, and 64 to 105 nm for NMC811 (Figure 7B). We have also noticed that materials with higher nickel content tend to form particles with a larger average size. By comparing the lowest and highest temperatures explored, the calculated crystallite size change is almost double. This dependency is consistent with the literature.^[29] Based on the values obtained, we conclude that the NMC crystallization process is generally inhomogeneous since all powders consist of partially small single crystallites and partially bigger polycrystalline particles. With increasing annealing temperatures, crystallites tend to further interconnect with bigger particles, and less of single crystallites are observed in SEM images. This change in particle and crystallite sizes and morphology may hold crucial implications for the electrochemical performance of the NMC materials,^[3,18] especially with the highest particle size distributions.

2.4. Electrochemical Investigation Concerning NMC Compositions and their Calcination Temperatures

To confirm the dependency of structural properties on electrochemical performance, chronopotentiometry tests have been conducted. As NMC can be seen as a material combining the advantages of LiCoO_2 , LiNiO_2 , and LiMnO_2 , we expect it to exhibit high operating voltage, large energy density, and relatively good cycling performance. Employing chronopotentiometry at different current loads enabled the determination of essential battery cycling parameters, including specific discharge capacity and cyclability expressed by capacity retention, defined as the ratio of the discharge capacity in the given cycle to the primary discharge capacity, expressed in percentage (Figure 7C and Table S1, Supporting Information). Additionally, evaluating the material's specific discharge capacity response provided insights into its discharge characteristics under high currents, holding significant relevance for applications involving unique current requirements.

All NMC111 samples performed quite well with the highest discharge capacity and the highest retention ($\approx 92\%$) for material calcined at 800°C , retaining 142.1 mAh g^{-1} at the last cycle and good retention at 1 C-rate of 84%. The sample annealed at 750°C showed the poorest performance among all three showing that for this composition the preferable calcination temperature is higher. When it comes to NMC622 the highest primary discharge

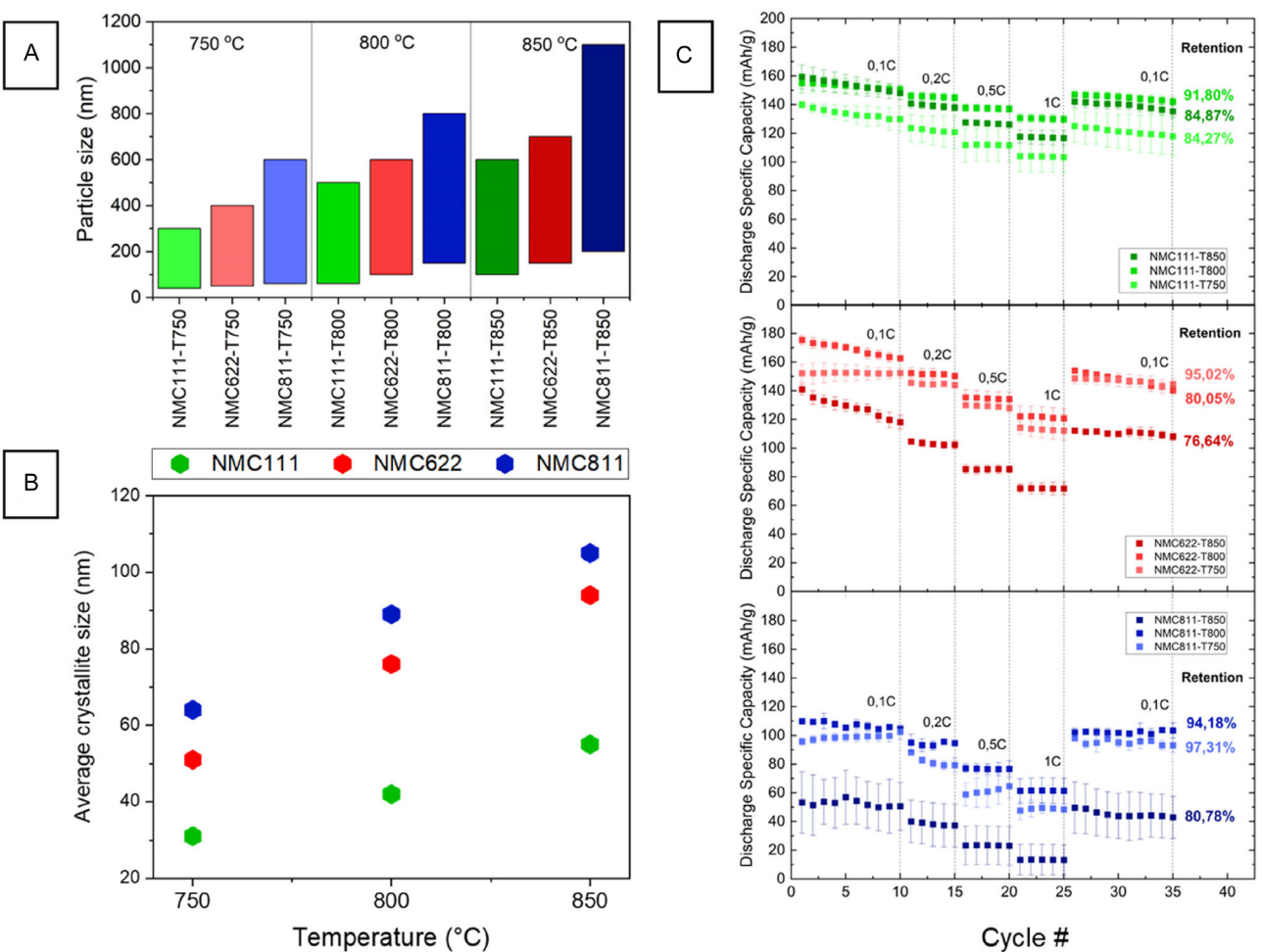


Figure 7. A) Particle sizes observed in SEM images and B) crystallite sizes obtained from the Scherrer equation. C) Chronopotentiometric high-rate test results of NMC 111 (2.9–4.3 V), NMC 622 (2.9–4.3 V), and NMC 811 (2.9–4.1 V).

capacity occurred for material calcined at 800 °C reaching 175.3 mAh g⁻¹ in the first cycle, but the most stable work with over 95% retention characterized the material synthesized at 750 °C, while maintaining reasonable discharge capacities (152.2–144.6 mAh g⁻¹) with 74% capacity retention at 1 C-rate and 95% after high rate tests. Finally, all NMC811 materials demonstrated stable operation due to diminished electrolyte decomposition effects by reducing potential window^[31,32] to maintain analogous properties as samples with lower Ni content. Although NMC811 exhibited rather low discharge capacities not higher than 110 mAh g⁻¹. Based on XRD and Raman results we see the structural limitations of those materials that affect its performance. This indicated a need to explore other annealing temperatures for Ni-rich NMC materials.

2.5. Influence of Calcination Atmosphere on Ni-Rich NMC

Since the NMC811 electrochemical performance was unsatisfying, we studied a few more calcination temperatures. We analyzed again the in situ XRD data and selected more regions for ex situ calcination. We chose 650 °C, which is the temperature

just before changing from stage III to stage IV; 700 °C, which is the temperature in the III → IV stage transition; and additionally 775 °C, which was the temperature where the doublets (018)-(110) and (006)-(012) separations seem to be the highest along in situ XRD measurement temperature range (**Figure 8A**).

The XRD patterns of the ex situ calcinated samples are shown in **Figure 8B**. The materials prepared at the lowest temperatures (650 and 700 °C) show the disordered hexagonal structure (stage III) and are electrochemically inactive (**Figure S10**, Supporting Information). The sample annealed at 775 °C showed different structural parameters than surrounded 750 and 800 °C showing a similar threshold as in situ XRD data. The grain size was 77 nm which fits into a trend for this sample, whereas *a* and *c* unit cell parameters were 2.875 and 14.212 Å, respectively (**Figure S11**, Supporting Information), which are the minimum values for air-calcinated NMC811 samples. Minima in *a*, *c*, and volume (*V*) parameters are observed for this sample, which shows a slight contraction in all three crystallographic directions. The (018) and (110) doublet separation is almost the same as for 750 and 800 °C. Thus, we can see that the electrochemical performance is slightly better for this sample (discharge capacity ≈118 mAh g⁻¹ in the initial cycles and 110 mAh g⁻¹ in the last one).

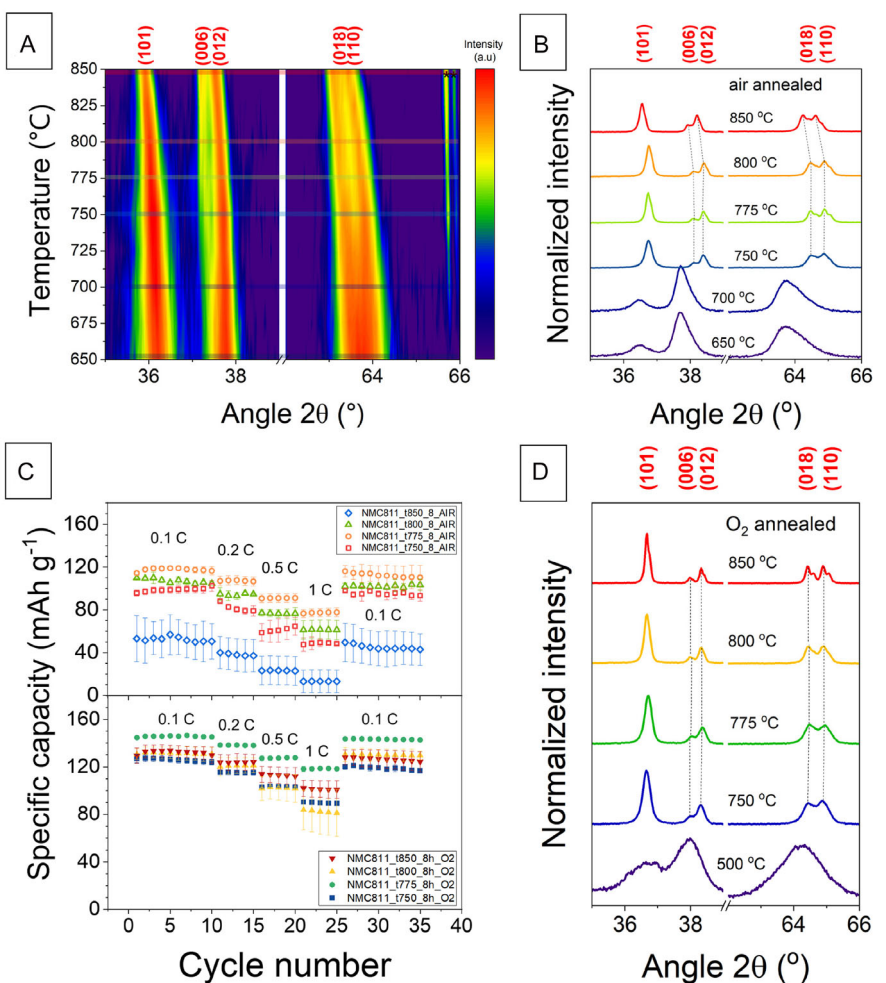


Figure 8. Comparison of in situ XRD heating A) with the ex situ XRD patterns B) prepared on NMC811 samples calcinated in air. C) Electrochemical performance of NMC811 materials calcinated at 750, 775, 800, and 850 °C in O₂ in comparison with air-annealed samples. D) XRD patterns of NMC811 calcinated in an O₂ environment at different temperatures.

Among many reports on NMC811 synthesis, we found several that used pure oxygen during the calcination. Thus, we have prepared four more samples annealed in O₂ and compared the results with air-calcinated analogs to find out the structural and electrochemical response differences. NMC811 tends to crystallize in a slightly different manner when calcinated in a pure oxygen environment. SEM images show that oxygen-annealed samples have smaller particle sizes (50 nm at 750 °C up to 500 nm at 850 °C) and less smooth facets and edges (Figure S12, Supporting Information). More rounded corners are also visible. There was a slow and progressive grain coarsening, but not at the level of air-annealed samples, which were double in size for all temperature ranges. Only 850 °C-annealed material showed a uniform particle size distribution of about 500 nm, showing a faster crystal growth between 800 and 850 °C.

Similarly to calcination in air, we also detected Li₂CO₃ crystals signal in the XRD pattern of 500 °C and O₂ annealed sample (below its melting temperature), and thus the suggestion that an amorphous layer of Li₂CO₃ is present in LiOH precursor before calcination^[17] was additionally confirmed in this study (Figure S13,

Supporting Information). The crystal size of the disordered NMC811 at this stage was ca. 8 nm. We also analyzed samples annealed at 750, 775, 800, and 850 °C, and as we expected none of those showed the existence of Li₂CO₃, since they are above the melting temperature of Li₂CO₃. Thus, we confirmed that the data shown in the work of Ying et al.^[17] had to be taken from the underheated sample by at least 77 °C (actual temperature of the material during scan close to 723 °C), and this is why Li₂CO₃ crystals were observed for 2 h at the set temperature of 800 °C. The disappearance of Li₂CO₃ can be connected to the final stabilization of the sample at the set temperature. This also suggests that NMC structural changes occurred with a similar delay to Li₂CO₃ melting, and it is uncertain whether the temperature reached the set 800 °C. The authors did not observe (006)-(012) doublet separation for NMC811, even after 10 h hold, which should appear at about 750 °C. For NMC111 the doublet separation should be well developed at the same temperature. This suggests that the temperature in the previously published experiment never reached 750 °C in both NMC111 and NMC811 in situ calcinations. This shows that

the heating rate in the synchrotron-based analysis should be carefully selected and the heating stage precisely calibrated. This challenge should be addressed in future fast-paced heating *in situ* experiments.

Similarly to SEM findings, crystallite sizes calculated using the Scherrer formula were smaller than air-annealed analogs up to 800 °C: in particular 39 nm for 750 °C (45% smaller), 58 nm for 775 (25% smaller), and 73 nm for 800 °C (22% smaller). This shows that up to 800 °C oxygen-rich atmosphere blocks the creation of bigger crystallites and hinders sintering into bigger polycrystalline particles. For 850 °C oxygen-annealed samples, we observed a grain size of 170 nm, which is about 57% bigger than air-annealed analog. When comparing the crystallographic parameters we see that oxygen-annealed samples are structurally closer to NMC622 (Figure S14, Supporting Information). What was also surprising, the oxygen-annealed NMC811 sample seemed to hold its hexagonal structure even at 850 °C. This was additionally confirmed using Raman mapping, where all four Raman maps showed very similar signals (Figure S15, Supporting Information). There were minor areas where a slight divergence was observed (especially at 850 °C annealed sample, where a few spectra showed early signs of the decomposition—the band at ca. 590 cm⁻¹ started to rise). Although the effect was minor compared to the air-annealed sample and thus we did not expect a significant change in electrochemical behavior.

As predicted, O₂ calcinated NMC811 materials had much better electrochemical performance than their air-annealed equivalents (Figure 8C and Table S1, Supporting Information). The sample annealed at 775 °C in O₂ showed the best electrochemical performance along both prepared data sets of NMC811. It showed ca. 142.8 mAh g⁻¹ of the specific capacity after 35 cycles, which is 99% of the capacity retention. The best air-annealed NMC811 sample showed on average only 110 mAh g⁻¹ (96%). It means that 26% of capacity improvement was achieved due to a change in the synthesis conditions. Overall, all oxygen-annealed samples outperformed their air-annealed analogs by at least 13% (for each annealing temperature—Figure S16, Supporting Information). Since the precursor used for both annealing types was the same, the reason for the structural and morphological differences lies only in the annealing atmosphere. As mentioned before the unit cell parameters were lowered, and thus the unit cell volumes remind of the NMC622 structure annealed at 800 °C. Similarly, the doublet (018) - (110) separation and those reflexes positions also were closer to the NMC622 structure. This shows that there is a unique order of atoms and their specific interatomic distances in the hexagonal layered structure that provide optimal diffusion pathways for lithium ions. Additionally, it seems that there is an optimal crystal size range (45–75 nm) at which NMC samples generally perform better.

When designing modified NMCs like core–shell structures, annealing temperature will significantly influence final material properties. The selected temperature and atmosphere will impact crystal growth in both Ni-rich cores and Ni-poor shells, determining whether optimal conditions for each hexagonal layered phase are achieved, directly affecting electrochemical performance. In

such a design, the crystal size gradient (bigger Ni-rich grains), crystal defects (unit cell parameter mismatch, thick grain boundaries, dislocations, etc.), particle shrinkage divergences (higher Ni-rich grain shrinkage), and other variations might be observed and might influence the final electrochemical behavior.

3. Conclusion

This work aimed to investigate the impact of calcination temperature on the structural, morphological, and electrochemical properties of NMC111, NMC622, and NMC811. For the first time, the conventional laboratory XRD machine was used to perform the *in situ* heating experiments of NMC precursors allowed to study of structural changes during annealing from room temperature up to 850 °C. Our findings shows that the annealing process is divided into four stages: 1) precursor hydroxides; 2) either spinel-like structure for low Ni content (stable up to 350 °C for NMC111) or cubic NiO-like phase for Ni-rich materials (stable up to 375 °C for NMC622, and 425 °C for NMC811); 3) disordered hexagonal; and 4) ordered hexagonal, formed at 650–700 °C. The excessive temperature led to degradation of Ni-rich NMCs, possibly transitioning back to rock salt structure. *In situ* VT-XRD guided the selection of calcination temperatures (750, 800, 850 °C) for ex situ testing. We also analyzed and discussed differences and advantages of using conventional XRD machines over synchrotron-based methods, especially in term of requirements for the stage calibration and heating rate, since those factors influence the result reliability.

Structural quality was assessed by XRD and SEM, showing increasing crystallite and particle size with temperature. This is also a first study using Raman mapping to detect the temperature-dependent crystal quality, homogeneity, and stability of the obtained powders. NMC111 showed consistent structure at all temperatures. NMC622 showed optimal results at 750 and 800 °C, while NMC811 displayed low hexagonal ordering and poor electrochemical performance when calcined in air. Materials demonstrated a higher primary discharge capacity for higher calcination temperatures—NMC111 for 850 °C, and NMC622 for 800 °C, although a significant capacity drop after 35 cycles was observed. Lower calcination temperatures of 750 °C for NMC622 and 800 °C for NMC111 induced the best structural quality and the most stable performance. Among those samples, NMC622 (750 °C) retained 144.6 mAh g⁻¹ discharge capacity (95% capacity retention). Air-calcined NMC811 retained only ≈110 mAh g⁻¹ after 35 cycles, but oxygen-annealed samples (structurally remaining of NMC622) achieved 142.7 mAh g⁻¹ with 98% capacity retention, confirming the importance of the calcination atmosphere.

The results obtained will be further used for the gradient structure material design based on a nickel-rich core. This study proved that the calcination temperature plays a crucial role in the NMC system development helping in stabilization of the hexagonal structure during cycling. Finally, it is concluded that the Li-ion battery based on NMC material could be safely applied once a precise tuning of the cell chemistry is achieved, resulting

in even safer and more reliable Li-ion batteries. In addition, this study serves as an example and shows materials scientists the applicability of laboratory *in situ* structural methods to their own research.

Supporting Information

The authors have cited additional references within the Supporting Information.^[32–39]

Acknowledgements

D.A.B., N.F., M.W.-S., K.G., and M.G. thank the support from the National Science Center in Poland through the Sonata 17 Programme (No. UMO-2021/43/D/ST5/03094).

Conflict of Interest

The authors declare no conflict of interest.

Data Availability Statement

The data that support the findings of this study are openly available in RepOD at <https://doi.org/10.18150/JKHCAM>, reference number 0.

Keywords: Raman spectroscopy · reaction mechanisms · solid-phase synthesis · solid-state structures · X-ray diffraction

- [1] N. Nitta, F. Wu, J. T. Lee, G. Yushin, *Mater. Today*, **2015**, *18*, 252.
- [2] G. E. Blomgren, *J. Electrochem. Soc.* **2017**, *164*, A5019.
- [3] A. C. Wagner, N. Bohn, H. Geßwein, M. Neumann, M. Osenberg, A. Hilger, I. Manke, V. Schmidt, J. R. Binder, *ACS Appl. Energy Mater.* **2020**, *3*, 12565.
- [4] H. J. Noh, S. Youn, C. S. Yoon, Y. K. Sun, *J. Power Sources* **2013**, *233*, 121.
- [5] H. Li, M. Cormier, N. Zhang, J. Inglis, J. Li, J. R. Dahn, *J. Electrochem. Soc.* **2019**, *166*, 1.
- [6] M. Roca-Ayats, M. Bianchini, P. Hartmann, T. Brezesinski, J. Janek, *Angew. Chem. -Int. Ed.* **2018**, *58*, 10434.
- [7] P. Hou, H. Zhang, Z. Zi, L. Zhang, X. Xu, *J. Mater. Chem. A Mater.* **2017**, *5*, 4254.

- [8] A. Manthiram, J. C. Knight, S. T. Myung, S. M. Oh, Y. K. Sun, *Adv. Energy Mater.* **2016**, *6*, 1501010.
- [9] A. A. Bunaci, H. Y. Aboul-enein, *Crit. Rev. Anal. Chem.* **2015**, *45*, 289.
- [10] Z. Feng, P. Barai, J. Gim, K. Yuan, Y. A. Wu, Y. Liu, V. Srinivasan, Y. Xie, *J. Electrochem. Soc.* **2018**, *165*, 3077.
- [11] M. Wolfman, X. Wang, J. C. Garcia, P. Barai, J. E. Stubbs, P. J. Eng, O. Kahvecioglu, T. L. Kinnibrugh, K. E. Madsen, H. Iddir, V. Srinivasan, T. T. Fister, *Adv. Energy Mater.* **2022**, *2102951*, 1.
- [12] M. Bianchini, F. Fauth, P. Hartmann, T. Brezesinski, J. Janek, *J. Mater. Chem. A Mater.* **2020**, *8*, 1808.
- [13] R. Weber, H. Li, W. Chen, C.-Y. Kim, K. Plucknett, J. R. Dahn, *J. Electrochem. Soc.* **2020**, *167*, 100501.
- [14] A. Tayal, P. Barai, H. Zhong, O. Kahvecioglu, X. Wang, K. Z. Pupek, L. Ma, S. N. Ehrlich, V. Srinivasan, X. Qu, J. Bai, F. Wang, *Adv. Mater.* **2024**, *36*, 2312027.
- [15] M. Duffiet, D. Goonetilleke, F. Fauth, T. Brezesinski, J. Janek, M. Bianchini, *Chem. Mater.* **2022**, *34*, 9955.
- [16] M. Wolfman, X. Wang, J. C. Garcia, P. Barai, J. E. Stubbs, P. J. Eng, O. Kahvecioglu, T. L. Kinnibrugh, K. E. Madsen, H. Iddir, V. Srinivasan, T. T. Fister, *Adv. Energy Mater.* **2022**, *12*, 2102951.
- [17] B. Ying, J. R. Fitzpatrick, Z. Teng, T. Chen, T. W. B. Lo, V. Siozios, C. A. Murray, H. E. A. Brand, S. Day, C. C. Tang, R. S. Weatherup, M. Merz, P. Nagel, S. Schuppler, M. Winter, K. Kleiner, *Chem. Mater.* **2023**, *35*, 1514.
- [18] J. Zheng, P. Yan, L. Estevez, C. Wang, J. G. Zhang, *Nano Energy* **2018**, *49*, 538.
- [19] M. Bianchini, F. Fauth, P. Hartmann, T. Brezesinski, J. Janek, *J. Mater. Chem. A Mater.* **2019**, *8*, 1808.
- [20] X. Zhang, A. Mauger, Q. Lu, H. Groult, L. Perrigaud, F. Gendron, C. M. Julien, *Electrochim. Acta* **2010**, *55*, 6440.
- [21] K. Wu, F. Wang, L. Gao, M. R. Li, L. Xiao, L. Zhao, S. Hu, X. Wang, Z. Xu, Q. Wu, *Electrochim. Acta* **2012**, *75*, 393.
- [22] T. Ohzuku, A. Ueda, M. Nagayama, *J. Electrochem. Soc.* **1993**, *140*, 1862.
- [23] J. R. Dahn, U. Von Sacken, C. A. Michal, *Solid State Ion.* **1990**, *44*, 87.
- [24] X. Zhang, W. J. Jiang, A. Mauger, F. G. Qiu, C. M. Julien, *J. Power Sources* **2010**, *195*, 1292.
- [25] J. N. Reimers, W. Li, J. R. Dahn, *Solid State Ion.* **2019**, *2738*, 123.
- [26] P. S. Whitfield, et al., *Solid State Ion.* **2005**, *176*, 463.
- [27] F. T. Geldasa, M. A. Kebede, M. W. Shura, F. G. Hone, Royal Society of Chemistry preprint, **2022**.
- [28] A. C. Wagner, N. Bohn, H. Geßwein, M. Neumann, M. Osenberg, A. Hilger, I. Manke, V. Schmidt, J. R. Binder, *ACS Appl. Energy Mater.* **2020**, *3*, 12565.
- [29] L. Tang, X. Cheng, R. Wu, T. Cao, J. Lu, Y. Zhang, Z. Zhang, *J. Energy Chem.* **2022**, *66*, 9.
- [30] J. Zhua, G. Chen, *J. Mater. Chem. A* **2019**, *7*, 5463.
- [31] A. Eldesoky, N. Kowalski, J. R. Dahn, *J. Electrochem. Soc.* **2023**, *170*, 080515.
- [32] J. Li, L. E. Downie, L. Ma, W. Qiu, J. R. Dahn, *J. Electrochem. Soc.* **2015**, *162*, A1401.

Manuscript received: May 16, 2025

Revised manuscript received: August 14, 2025

Version of record online: